Astron. Astrophys. 322, 73–85 (1997)

ASTRONOMY
AND
ASTROPHYSICS

Modeling extragalactic bowshocks

I. The model

P. Ferruit[1], **L. Binette**[2,1], **R.S. Sutherland**[3], **and E. Pécontal**[1]
[1] Observatoire de Lyon, UMR CNRS 5574, 9 av. Charles André, F-69561 Saint-Genis-Laval Cedex, France
[2] European Southern Observatory, Casilla 19001, Santiago 19, Chile
[3] The Astrophysical Theory Centre, The Australian National University, Private Bag, Weston Creek P.O, ACT 2611, Australia

Received 31 August 1996 / Accepted 18 November 1996

Abstract. To probe the effects of the nuclear activity on the host galaxy, it is essential to disentangle the relative contribution of shock excitation from that of photoionization. One milestone towards this goal is the ability to model the bowshock structures created by the interaction of radio ejecta with their surrounding medium. We have built a bowshock model based on TDA's one (Taylor, Dyson & Axon 1992) which was itself derived from an earlier work on Herbig-Haro objects. Since TDA's original model supplied the astronomers with only [O III]λ5007 fluxes and profiles for various models of bowshocks, we undertook to include magnetic fields and to incorporate all of the atomic data tables of the code MAPPINGS IC for the computation of ionization states, cooling rates and line emissivities of the gas. This new model allows us to map line ratios and profiles of extragalactic bowshocks for all major lines of astrophysical interest. In this first paper, we present our model, analyse the gas behavior along the bowshock and give some examples of model results.

Key words: galaxies: active; ISM – shockwaves

1. Introduction

Many studies of the origin of the excitation of the emission line gas surrounding active galaxy nuclei often aim at confirming photoionization by either counting the number of ionizing photons available (e.g. Binette et al. 1985) or by probing the anisotropy of the nuclear ionizing radiation (Wilson et al. 1994; Acosta-Pulido et al. 1990; Acosta-Pulido 1993) through the observation of structures like the ionization cones. On the other hand most of the objects with extended narrow line regions (ENLR) exhibit radio jets or plasmons (Wilson & Tsvetanov 1994 and references therein) which may contribute to the heating and ionization of the gas as well as to its spatial distribution. Extensive works on the interaction between these radio ejecta (jets, plasmons) and their surrounding gas have followed two radically different approach: on one hand, there were pure hydrodynamical simulations, essentially dedicated to radio-galaxies and addressing the problem of the radio emission (e.g. see Coleman & Bicknell 1985; Higgins et al. 1995; Steffen et al. 1996); on the other hand, there where the planar steady-state shock models intended to model the line ratios and incorporating an exhaustive handling of the ionization, emission and transfer processes (Contini & Aldrovandi 1983, 1986; Viegas-Aldrovandi & Contini 1989; Sutherland et al. 1993, Dopita & Sutherland 1995, 1996). As a result of their incomplete description of the atomic processes, the former do not provide maps of line fluxes, ratios or line profiles to compare with the observations. On the contrary, the latter provide very complete sets of line diagnostics but lack any structural or kinematic information.

Simple models of the interaction of a plasmon and the ISM gas, either in the expansion dominated stage (Pedlar et al. 1985) or in the bowshock dominated one (Taylor, Dyson & Axon 1992, hereafter TDA), have been developed to fill this gap. These models, however, considered only the [O III]λ5007 line and provided only a few diagnostics (the [O III] line profile and flux, the shift between radio and [O III] emissions). To alleviate such limitations, we have undertaken to build a model of extragalactic bowshocks (e.g. such as expected in Seyfert galaxies) based on the hydrodynamical description of TDA but which can handle the presence of magnetic field as well as consider an exhaustive set of atomic processes such as those contained in the multipurpose shock/photoionization code MAPPINGS IC (see description in Appendix A). The pioneering work of TDA is now extended to cover most of the astrophysically interesting elements and lines. Our model includes a time dependent ionization balance, an updated atomic data set and a wide range of ionization processes, all of which has led to a much more reliable computation of the ionization state and line emissivities.

In this paper, we first give a detailed description of our model. We then describe the behavior of a test particle dur-

Send offprint requests to: P. Ferruit: ferruit@obs.univ-lyon1.fr

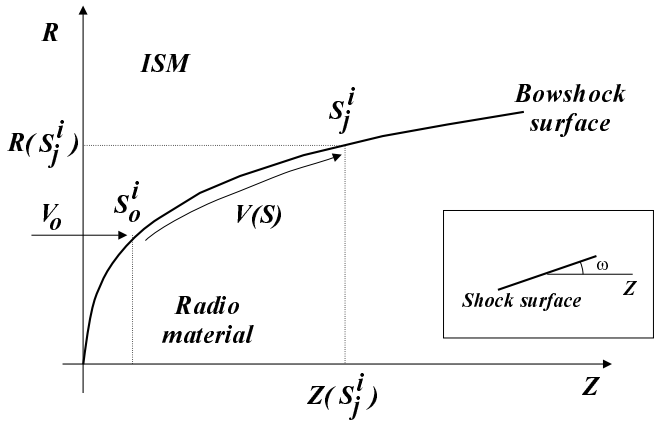

Fig. 1. Drawing of the model geometry in the bowshock frame (the ambient medium moves in the Z-direction with the velocity V_o). An annular fluid particle (the i^{th}) enters the bowshock at the curvilinear abscissa S_0^i and then flows along the shock surface. At the j^{th} time step of its evolution, it has reached the curvilinear abscissa S_j^i.

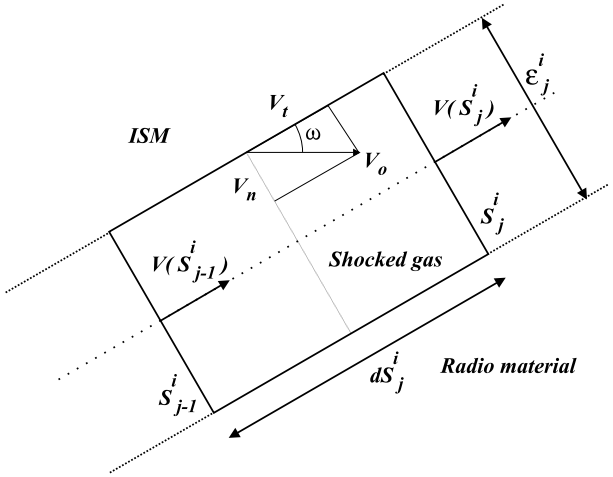

Fig. 2. Sketch of the jth fluid cell of the ith particle.

ing its evolution, showing the effects of different hydrodynamical assumptions. Last, we illustrate the results produced by the complete model with three examples. The characteristics of MAPPINGS IC are reviewed in Appendix A. Grids of line ratios and profiles for various bowshocks will be presented in a second paper.

2. Model description

This model, based on TDA's one, is a simple Lagrangian description of the bowshock structures which are expected to occur in active galaxies. The bowshock is assumed to be stationary and axi-symmetric. We will therefore use the cylindrical coordinates (R, Z, θ), the Z-axis being the axis of symmetry. All quantities are given in the bowshock surface frame.

2.1. Gas metallicity

We adopt a fixed He/H abundance ratio of 0.1. The abundance set (by number) of metals relative to H is the following:
C, N, O, Ne, Mg, Si, S, Ar, Ca, Fe : H = $10^{-6}\mathscr{Z}\times$
(363, 112, 851, 123, 38.0, 35.5, 16.2, 3.63, 2.29, 46.8),
respectively. The metallicity $\mathscr{Z}$ is simply a scaling factor. Unless specified otherwise, we assume $\mathscr{Z}$ = 1, which corresponds to the solar metallicity abundance set of Anders & Grevesse (1989). We assume the gas is dust free as we expect that dust would be rapidly destroyed in the very hot post-shock zone considered here.

2.2. Surrounding medium and nuclear source

The surrounding medium in which the bowshock propagates (which in most of the cases will be the ISM of the host galaxy) is assumed to have reached thermal and ionization equilibria and to be homogeneous with a filling factor of unity. It is illuminated by a nuclear ionizing source [power law with a spectral index κ ($f_\nu \propto \nu^\kappa$)]. The ionization parameter, a measure of the excitation level of the ionized gas, is defined as the ratio of the density of ionizing photons to the gas hydrogen number density:

$$\mathscr{U}_o = \frac{\int_{\nu_o}^{\infty} f_\nu d\nu/h\nu}{c\, n_o}$$

where f_ν is the monochromatic ionizing energy flux at the distance of the bowshock's head, ν_o the ionization potential of H, n_o the hydrogen number density of the ambient medium gas and c the speed of light. For definiteness, we adopt the canonical index $\kappa = -1.4$ as in TDA.

To avoid introducing poorly constrained parameters, we have assumed that the ionization parameter $\mathscr{U}_o$ of the unshocked gas is constant (i.e. we neither account for spatial variation in geometrical dilution of the nuclear radiation, nor for additional ionizing radiation generated *in situ* by the hot shocked gas [see Sect. 4.5.2]). Once the abundances and κ are set, this leaves us with the two remaining free parameters $\mathscr{U}_o$ and n_o. Note that in the low density regime and in the absence of magnetic field, line ratios are weakly dependent on the explicit values of n_o and κ. The equilibrium ionization balance of the ambient medium and its temperature are computed using MAPPINGS IC (see Appendix A).

2.3. Geometry

The layer of shocked gas is assumed to be thin compared to the characteristic size of the bowshock. Therefore, we do not distinguish between the bowshock surface and the interface with the radio material. We use the same fixed geometry than TDA for the bowshock surface (see Fig. 1), with a profile:

$$Z = \alpha R^2 + \psi R^4 = \frac{C}{D_Z} R^2 + \frac{1-C}{D_Z^3} R^4$$

where C and D_Z (input parameters for the model) are defined in TDA (the first one has been labeled C instead of B, to avoid

confusion with the magnetic field). The curvilinear abscissa S along the bowshock surface is then derived using:

$$dS = \left[1 + \left(\frac{dZ}{dR}\right)^2\right]^{\frac{1}{2}} dR = \left[1 + \left(\chi R + \delta R^3\right)^2\right]^{\frac{1}{2}} dR$$

where $\chi = 2\alpha$ and $\delta = 4\psi$. The sine of the angle ω between the normal to the interface and the Z-axis (see sketch in Fig. 1) is then:

$$\sin\omega = \left[\frac{1}{1 + \left(\chi R + \delta R^3\right)^2}\right]^{-\frac{1}{2}} \quad \text{with} \quad 0 \leq \omega \leq \frac{\pi}{2}$$

2.4. Post-shock conditions

The oblique shock geometry is shown in Fig. 2. In our stationary model, the gas velocity component normal to the interface must be zero after the shock. We have assumed that this occured in two steps. First, just behind the shock front, the conversion into pressure of the momentum component normal to the interface is partial and yields the usual Rankine-Hugoniot relations for an oblique, adiabatic shock with or without frozen-in magnetic field. In a subsequent step, all the remaining momentum normal to the interface is converted adiabatically (as in the first stage), instead of isothermally as assumed in TDA. This requires that the transverse move during this conversion remains sufficiently small that we can neglect any longitudinal changes in the physical parameters. Note, that this holds as long as the thin shock layer assumption does.

Once the post-shock pressure and density known, the post-shock temperature is computed using the perfect gas law. The ionic populations are assumed to remain unchanged through the shock interface (thin shock layer assumption), leading to an out of equilibrium state consisting of a very high temperature but low excitation (relative to equilibrium case) gas. A plot of the post-shock temperature and density as a function of the isothermal Mach number $\mathscr{M}$ is displayed in Fig. 3.

2.4.1. Case without magnetic field

Without magnetic field, the derived post-shock conditions for a perfect gas with a specific heat ratio γ are the following (all quantities labeled with "o" refer to the unperturbed ambient medium; V_o is the plasmon velocity):

$$P_{PS}(S) = P_o \left[1 + \mathscr{M}^2(S)\right]$$

$$\rho_{PS}(S) = \rho_o\, \Omega(S) \left[\frac{1 + \mathscr{M}^2(S)}{1 + (1 - 1/\Omega(S))\mathscr{M}^2(S)}\right]^{1/\gamma}$$

$$\mathscr{M}^2(S) = \frac{\rho_o V_o^2 \sin^2\omega(S)}{P_o}$$

$$\Omega(S) = \frac{(\gamma+1)\mathscr{M}^2(S)}{(\gamma-1)\mathscr{M}^2(S) + 2\gamma}$$

where $\Omega(S)$ is the post-shock compression factor and $\mathscr{M}(S)$ the isothermal Mach number.

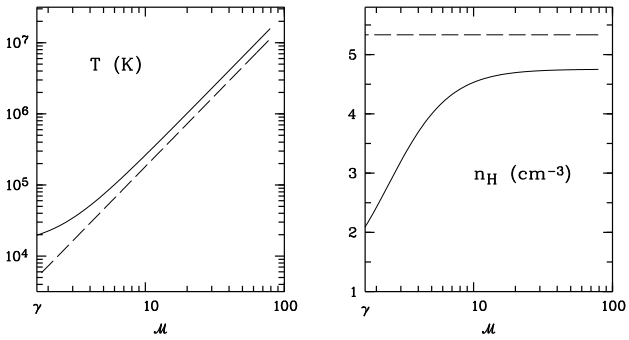

Fig. 3. Post-shock temperature (left panel) and hydrogen number density (right panel) as a function of the isothermal Mach number $\mathscr{M}$ derived from TDA's model (dashed line) and from our set of equations (solid line). The initial density, temperature and magnetic parameter were, 1 cm^{-3}, 9 10^3 K and 3 μG cm$^{3/2}$. The specific heat ratio of the gas was γ=5/3. Note, at high Mach numbers, the systematic shift between the results of the two models. This is due to our choice of adiabatical conversion of the residual normal momentum instead of the isothermal conversion assumed by TDA. In the small Mach number range (typically $M < 10$), TDA's strong shock assumption breaks down which explains why the two curves rapidly separate.

2.4.2. Case with magnetic field

We have assumed that both B_o^n (normal to the bowshock surface) and B_o^l (longitudinal to the bowshock surface) ambient magnetic field components have the same amplitude along the whole bow shape. They have been taken to be (Dopita & Sutherland 1995):

$$\left[\frac{B_o^n}{\mu\mathrm{G}}\right] = \left[\frac{B_o^l}{\mu\mathrm{G}}\right] = \mathscr{B}_o \times \left[\frac{n_o}{\mathrm{cm}^{-3}}\right]^{1/2}$$

with the magnetic field parameter $\mathscr{B}_o$ ranging from 0 to 5 μG cm$^{3/2}$.

The Rankine-Hugoniot post-shock compression factor $\Omega_{RH}(S)$ is the positive real solution of the following second order equation (all quantities labeled with "o" refer to the unperturbed surrounding medium):

$$a\,\Omega_{RH}^2 + b(S)\,\Omega_{RH} + c(S) = 0$$
$$a = 2(2-\gamma)\beta_o \qquad c(S) = (\gamma+1)\mathscr{M}_o^2(S)$$
$$b(S) = (\gamma-1)\mathscr{M}_o^2(S) + 2\gamma(1+\beta_o)$$

with

$$\Omega_{RH}(S) = \rho_{RH}(S) \,/\, \rho_o$$
$$\beta_o = \frac{\left[B_o^l\right]^2}{8\pi\, P_o} \qquad \mathscr{M}_o^2(S) = \frac{\rho_o V_o^2 \sin^2\omega(S)}{P_o}$$

The Rankine-Hugoniot post-shock pressure and magnetic field then yield:

$$B_{RH}^l(S) = \Omega_{RH}(S)\, B_o^l \quad \text{and} \quad B_{RH}^n(S) = B_o^n$$

$$P_{RH}(S) - P_o \;=\; P_o \times \left[\left(1 - \frac{1}{\Omega_{RH}(S)}\right) \mathscr{M}_o^2(S) + \beta_o \left(1 - \Omega_{RH}^2(S)\right)\right]$$

The adiabatic compression factor $\Omega_{ad}(S)$ associated with the adiabatic conversion of the remaining normal kinetic energy into ram-pressure is computed by solving numerically the equation:

$$\beta_{ad}(S)\,\Omega_{ad}^2 \;+\; \Omega_{ad}^{\gamma} \;-\; \left[1 + \mathscr{M}_{ad}^2(S) + \beta_{ad}(S)\right] \;=\; 0$$

with (ρ_{PS} beeing the final post-shock density)

$$\Omega_{ad}(S) \;=\; \rho_{PS}(S) \,/\, \rho_{RH}(S)$$
$$\beta_{ad}(S) \;=\; \frac{\left[B_{RH}^l(S)\right]^2}{8\pi\, P_{RH}(S)}$$
$$\mathscr{M}_{ad}^2(S) \;=\; \frac{\rho_{RH}(S) V_{RH}^2(S)}{P_{RH}(S)} \;=\; \frac{\rho_o V_o^2 \,\sin^2\omega(S)}{\Omega_{RH}(S)\, P_{RH}(S)}$$

The final post-shock pressure and magnetic field (all quantities label with PS refer to the final post-shock conditions) yield:

$$P_{PS}(S) \;=\; P_{RH}(S)\,\Omega_{ad}^{\gamma}(S)$$
$$B_{PS}^l(S) \;=\; B_{RH}^l(S)\,\Omega_{ad}(S) \;=\; B_o^l\,\Omega_{ad}(S)\,\Omega_{RH}(S)$$
$$B_{PS}^n \;=\; B_{RH}^n \;=\; B_o^n$$

2.5. Total pressure and velocity fields

Following TDA, all the particles sharing the same curvilinear abscissa S are assumed to be in mechanical equilibrium. We can therefore derive the total pressure $\Phi(S)$ (sum of the gas and magnetic pressures) and velocity fields (along the bowshock surface) using the post-shock total pressure $\Phi_{\rm PS}$ and the conservation laws of longitudinal momentum and mass. This gives:

$$\Phi(S) \;=\; \Phi_{\rm PS}(S) \;=\; P_{PS}(S) \;+\; \frac{\left[B_{PS}^n\right]^2 + \left[B_{PS}^l\right]^2}{8\pi}$$
$$V(S) \;=\; \frac{2V_o}{R(S)^2} \int_0^S R(s)\sin\omega(s)\cos\omega(s) ds$$

where V_o is the bowshock velocity.

2.6. Particle evolution

In this section, we describe the step by step computation of the evolution of the fluid which entered the bowshock through the i^{th} annulus of curvilinear abscissa S_0^i and length dS_0^i (quantities refering to the j^{th} time step of the evolution of this i^{th} particle are labeled using the upperscript i and the subscript j).

2.6.1. Temperature, density and magnetic field evolution

After the shock discontinuity, the particle flows along the surface of the bowshock. We assume that it does not interact thermally with the other particles. Writing the internal energy density conservation law for the particle (Shapiro et al. 1992) and using the perfect gas equation of state, we derive the relation used by TDA to compute the temperature evolution:

$$\frac{dT}{T} \;=\; \left(\frac{\gamma - 1}{\gamma}\right) \;\times\; \left(\frac{dP}{P} \;-\; \frac{dQ}{P}\right)$$

where dQ is the net cooling of the gas (losses minus gains).

Along the flow, the total pressure and the frozen-in magnetic field of the gas particle yield the relations:

$$d\Phi \;=\; dP \;+\; \frac{1}{4\pi}\left(B^n\, dB^n \;+\; B^l\, dB^l\right) \;=\; d\Phi_{PS}$$
$$\frac{dB^n}{B^n} \;=\; \frac{d\rho}{\rho} \quad \text{and} \quad dB^l \;=\; 0$$

This gives the particle temperature evolution relation:

$$\frac{dT}{T} \;=\; \frac{(\gamma - 1)(1 + 2\beta)}{2\beta + \gamma} \left[\frac{d\Phi_{PS}}{(1 + 2\beta)P} \;-\; \frac{dQ}{P}\right]$$
$$\beta \;=\; \frac{B^2}{8\pi\, P}$$

Therefore, the temperature of the i^{th} fluid particle at the j^{th} time step is computed step by step using the recursive equation (similar relations can be derived for the pressure, density and normal magnetic field):

$$T_0^i \;=\; T_{\rm PS}(S_0^i)$$
$$T_j^i - T_{j-1}^i \;=\; \left(\frac{(\gamma - 1)(1 + 2\beta_{j-1}^i)}{2\beta_{j-1}^i + \gamma}\right) \frac{T_{j-1}^i}{P(S_{j-1}^i)} \times \left[\frac{\Phi_{PS}(S_j^i) - \Phi_{PS}(S_{j-1}^i)}{1 + 2\beta_{j-1}^i} \;-\; \frac{dS_j^i}{V(S_j^i)} \left(\frac{dQ}{dt}\right)_{j-1}^{i}\right]$$
$$\beta_{j-1}^i = \frac{[B^n]_{j-1}^i \times [B^n]_{j-1}^i}{8\pi\, P(S_{j-1}^i)}$$

where $dQ/dt = \Lambda - \Gamma$ is the total net cooling rate of the gas in erg s^{-1} cm^{-3}. As we do not assume ionization equilibrium but compute explicitly the temporal evolution of the ionization balance using MAPPINGS IC routines, the cooling rate depends on the particle's ionization 'history' as well as on its temperature and density. Note that all these relations assume that the mean molecular weight of the gas particle remains constant during the step. In fact, its change is computed *a posteriori*, once the new ionization state of the fluid known.

2.6.2. Ionization state

The ionization state of the particles is computed with MAPPINGS IC by solving the time dependent ionization balance set

of equations (Binette et al. 1985). Briefly, the heavy element ionization balance equations are expressed in a matrix form:

$$\frac{d\boldsymbol{\sigma}}{dt} = \mathsf{R}\,\boldsymbol{\sigma}$$

where $\boldsymbol{\sigma}$ is the column vector containing the ionic abundances and R is the matrix containing the rates per ion (s^{-1}) corresponding to the various changes in ionization stage allowed for the atomic element under consideration (see Appendix A). If we assume that the rates remain constant during some timestep t, then the ionic abundances at the end of the time step, $\boldsymbol{\sigma}_f$, are given in terms of the abundances at the start, $\boldsymbol{\sigma}_s$, by the matrix equation:

$$\boldsymbol{\sigma}_f = e^{\mathsf{R}t}\,\boldsymbol{\sigma}_s$$

In the case of hydrogen, however, it is necessary to solve the ionization balance separately and in an analytical form since the electron density (used in determining the recombination and collisional ionization rates) is itself directly proportional to the fractional ionization of hydrogen. The mode assumes the *on-the-spot* approximation (Osterbrock 1989) in the processing of the local diffuse field in the interest of simplicity (see Sect. 4.5.2).

The elapsed time dt_j^i between two steps is estimated using the particle velocity $V(S_j^i)$ and the curvilinear abciss change dS_i^j (i^{th} particle, j^{th} time step). If dt_j^i is too long to consider R as a constant matrix (as a result of rapid variations in temperature, total or electronic density), the timestep is divided into smaller time intervals with successive updating of R.

2.6.3. Adaptive stepsize

As the fluid flows along the bowshock surface, it crosses various regions characterized by very different evolution time scales. To save computation time without loosing accuracy, we have used a varying curvilinear abscissa stepsize. The stepsize control is achieved through a maximum allowed change rate based on four tolerance parameters (temperature, total pressure, velocity and mass density times the velocity). We have also added an absolute maximal change in velocity which is set using the expected velocity sampling of the final model output. The setting procedure of these tolerance parameters is described in Sect. 4.1.

2.7. Bowshock sampling

We have furthermore used an adaptive stepsize for the bowshock sampling. We have monitored two parameters, the velocity and the Z position of the sharp cooling zone (see Sect. 3.2). This was done to ensure that the final samplings in velocity and in Z were high enough for the astrophysical purpose of the modeling.

2.8. Line fluxes

To derive the flux emitted by the i^{th} particle ($i \geq 1$; $i = 0$ corresponding to the coordinates of the bowshock apex) as it flows and cools, we need to know its depth (radial extension) $\mathscr{E}_j^i$ and its volume $\mathscr{J}_j^i$. From mass conservation relations, we derive ($j \geq 1$):

$$\begin{aligned}
\mathscr{E}_0^i &= \frac{R(S_0^{i-1}) + R(S_0^i)}{2\,R(S_0^i)}\,\frac{\rho_o V_o}{\rho_{\rm PS}(S_0^i)V(S_0^i)}\,\sin\omega(S_0^i)\,dS_0^i \\
\mathscr{E}_j^i &= \left(1 - \frac{\rho(S_j^i)V(S_j^i) - \rho(S_{j-1}^i)V(S_{j-1}^i)}{\rho(S_j^i)V(S_j^i)}\right)\,\mathscr{E}_{j-1}^i \\
\mathscr{J}_0^i &= \pi\,\left[R(S_0^{i-1}) + R(S_0^i)\right]\,\mathscr{E}_0^i\,dS_0^i \\
\mathscr{J}_j^i &= \pi\,\left[R(S_{j-1}^i) + R(S_j^i)\right]\,\mathscr{E}_j^i\,dS_j^i
\end{aligned}$$

The line emissivities for a given temperature, density and ionic populations are computed using MAPPINGS IC.

3. Analysis of a single particle evolution

This section is dedicated to a careful examination of the evolution of a test particle.

3.1. Parameters defining the shock

For comparison purposes, we adopt the same particle as in TDA, i.e. a particle entering their model labeled E at Z =1 pc. The bowshock parameters are then: C = 0.6, D_Z = 40 pc, V_o = 700 km.s^{-1}, n_o = 1 cm^{-3} and $\mathscr{B}_o$ = 0.012. The ionization parameter we inferred from TDA is derived from their value of the nuclear ionizing flux (i.e., a luminosity of 10^{43} erg s^{-1}) in the range $0.5-4.5$ keV, a continuum with $\kappa = -1.4$ and an apex distance to the nucleus of 500 pc). The magnetic parameter of the ambient medium has been set to $\mathscr{B}_o$ = 3 μG cm$^{3/2}$.

3.2. The evolution scheme

The evolution of a particle along the bowshock can be divided into several stages according to the locally prevailing physical process. Note that the relative lengths and importances of each stage vary from particle to particle and depend as well on the bowshock parameters. We distinguish the following stages:

3.2.1. Thermal ionization stage.

Just after being shocked, the particle still has the same ionization state as the ambient gas while having reached a temperature beyond 10^6 K. A fraction of the thermal energy of the gas is being used to raise the ionization level. This leads to an extremely high initial cooling rate (see Fig. 4). This stage is very short (less than 0.5 pc in curvilinear abscissa, i.e. less than 5.10^3 yr) as the particle rapidly reaches ionization levels consistent with its temperature (see Fig. 5).

3.2.2. Pressure driven stage.

Once the ionization stage ends, the gas retrieves the low radiative cooling rates typical of a hot, low density plasma. Therefore,

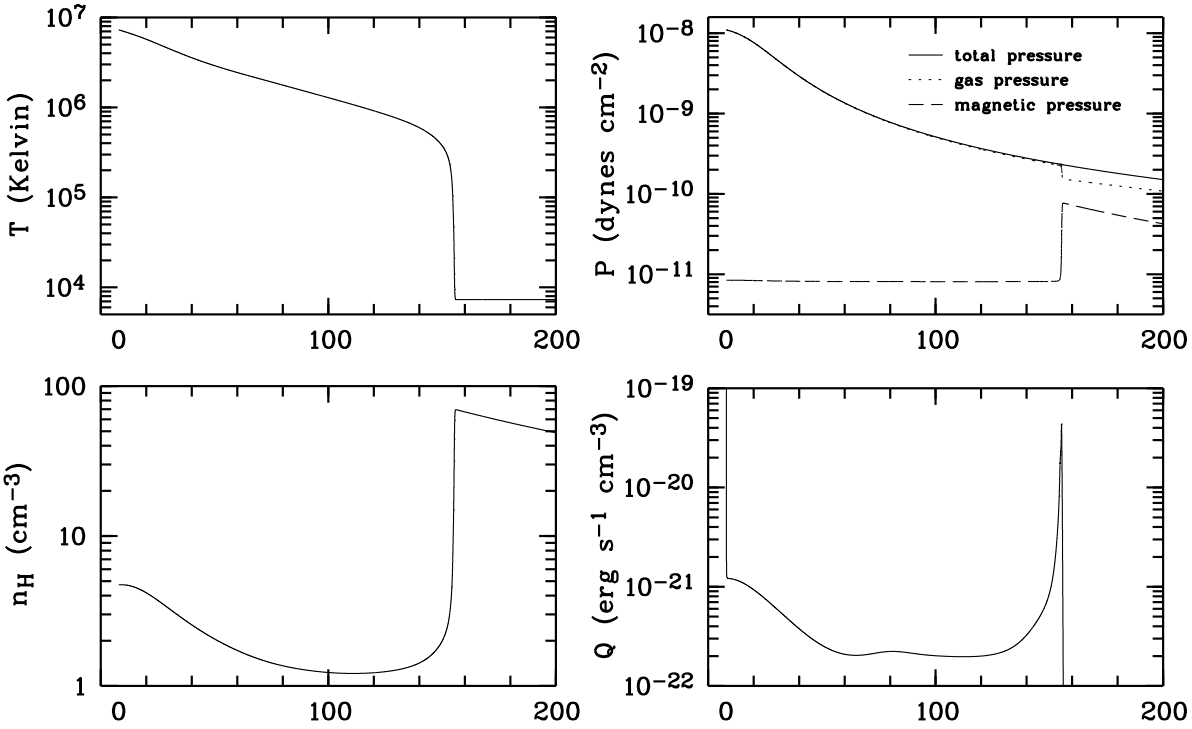

Fig. 4. Evolution tracks of the temperature, pressures (total, gas and magnetic), hydrogen number density and radiative cooling rate per volume unit for our test particle. Note the steep increase in hydrogen number density and magnetic pressure during the catastrophic cooling stage ($S \simeq 160$ pc).

the cooling of the particle is ruled by the decreasing pressure field. In this pressure driven stage, the gas cools slowly as its pressure and density decrease. The length of this region depends strongly on the initial temperature and density of the particle. Note, that for the extreme case of very high velocity bowshocks in low density surrounding gas, the density decrease can actually inhibate the radiative cooling term (which varies roughly as the square of the density), leading to very extended pressure driven stages.

3.2.3. Catastrophic cooling stage.

As the temperature falls and reaches a few 10^5 K, the radiative cooling engine races. The temperature decrease is not balanced any more by the pressure decrease, which leads to a fast increase in density which itself accelerates the cooling and so depresses ever more rapidly the temperature. The final compression factor of the gas is determined by the magnetic field whose pressure (which varies as the square of the density) can in some cases dominate the gas pressure. During this catastrophic cooling stage, the gas cools down to temperatures around 5 10^3-10^4 K within a few parsecs only, releasing radiatively within a very thin zone what remains of its thermal energy. The salient features of this stage are seen in the T, n_H, P and Q curves of Fig. 4 (around S = 160 pc).

3.2.4. Photoionization stage.

The cool, high density gas leaving the catastrophic cooling zone rapidely reaches thermal equilibrium (balance between radiative cooling and photoionization heating by the nuclear radiation). The density decreases slowly (n_H tightly follows the pressure evolution as the temperature is set by the thermal balance). Therefore, the ionization parameter of the gas increases and the thermal equilibrium moves slowly toward higher temperatures and higher excitation populations (quasi-static evolution).

3.3. Ionic populations and line emissivities

The 'mean ionization'[1] degree of several elements (O, N, C, Fe, Ca and Mg) as a funtion of the curvilinear abscissa is given in Fig. 5, together with the individual ionic fraction of three ions of astrophysical interest covering a wide range of excitation (Fe XIV, Fe VII and O III). Prominent features in these curves are: the spike (at the beginning) associated with the thermal ionisation stage and the fast change of population related to the catastrophic cooling stage ($S \approx 160$ pc). It is worth noticing the importance of the photoionization stage in the luminosity profile (see Fig. 5) of intermediate and low excitation lines.

[1] For each atom we simply average together all of its ionization fractions.

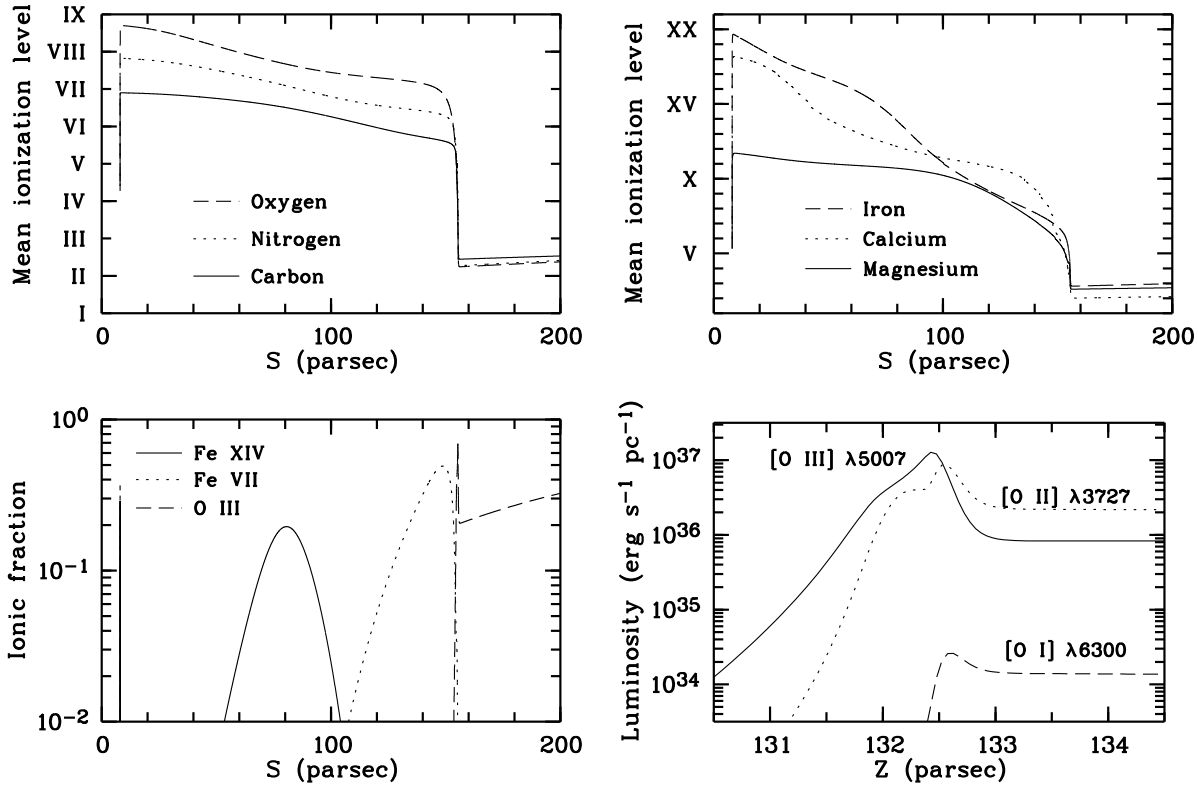

Fig. 5. *Top diagrams*: mean ionization levels of various elements for our test particle (left: carbon, nitrogen and oxygen; right: iron, calcium and magnesium) as a function of the curvilinear abscissa. *Lower, left panel*: ionic fraction of Fe XIV, Fe VII and O III as a function of the curvilinear abscissa. *Lower, right panel*: luminosity per unit of Z (integrated over the whole perimeter of a bowshock transversal slice) in the [O III]λ5007, [O II]$\lambda\lambda$3727 and [O I]λ6300 lines (zoom over the catastrophic cooling zone).

3.4. Cooling length

As the catastrophic cooling zone (see Sect. 3.2.3) is associated with a large increase in density, we have defined the cooling position of a particle, $Z_{\rm cooling}$, as the location of its maximum density. The cooling length $\mathscr{L}_{\rm cooling}$ is then derived using $\mathscr{L}_{\rm cooling} = Z_{\rm cooling} - Z_{\rm shock}$ where $Z_{\rm shock}$ is the position of the shock discontinuity (projected on Z) for the particle under consideration. As shown in the previous section, $Z_{\rm cooling}$ corresponds to a zone of enhanced emission which influences the final position of the bulk of the optical emission (and therefore the shift between radio and optical emission).

To make a more direct comparison with TDA, we have configured another test model which conforms strictly to TDA's model by using the same cooling rates, post-shock assumptions and the pure, fully ionized hydrogen assumption (i.e., $n_e \equiv n_H$). The derived temperature and hydrogen number density tracks are displayed in Fig. 6. Note that we exactly recover their curves (see their Fig. 4; model E, particle with $Z_{\rm shock} = 1$ pc), successfully testing the hydrodynamical routines of our code.

The striking difference between the evolutionary tracks of our complete model (Figs. 4 and 5) and those of TDA (Fig. 6) in which simplified physical assumptions have been used is noteworthy. For instance, for the same test particle, our complete model and TDA's one lead to $\mathscr{L}_{\rm cooling}$ values as different as 133.2 and 57.4 pc, respectively. This important difference in a key quantity is due to the cumulative effects of modified post-shock conditions (see Sect. 3.5) and different cooling rates.

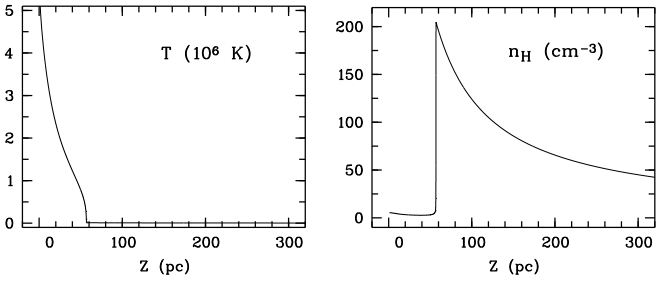

Fig. 6. Temperature and hydrogen number density as a function of Z for a particle with $Z_{\rm shock} = 1$ pc in the case of a simplified model which strictly conforms to TDA's model E (see their Fig. 4). Bowshock parameters: $B = 0.4$, $D_Z = 40$ pc, $V_o = 700$ km.s^{-1}, $n_o = 1$ cm^{-3}, $\mathscr{U}_o = 0.01$ and $\mathscr{B}_o = 0$ μG cm$^{3/2}$.

3.5. Influence of post-shock conditions equations

Our set of post-shock condition equations differs from the one of TDA (see Sect. 2.4). This leads, for a given Mach number, to

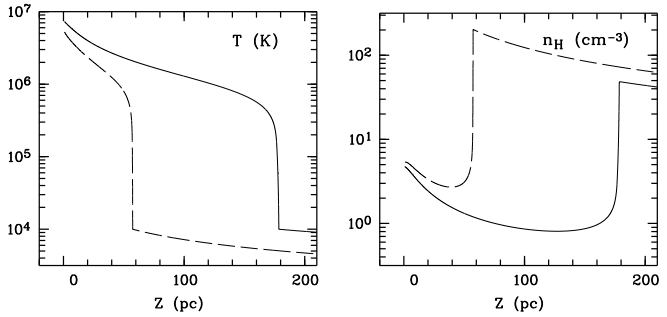

Fig. 7. Comparison between TDA's model E (dashed line; same model as in Fig. 6) and our model when configured to use TDA's cooling function (solid line). The magnetic parameter of the ambient medium has been set to zero as in the model of Fig. 6.

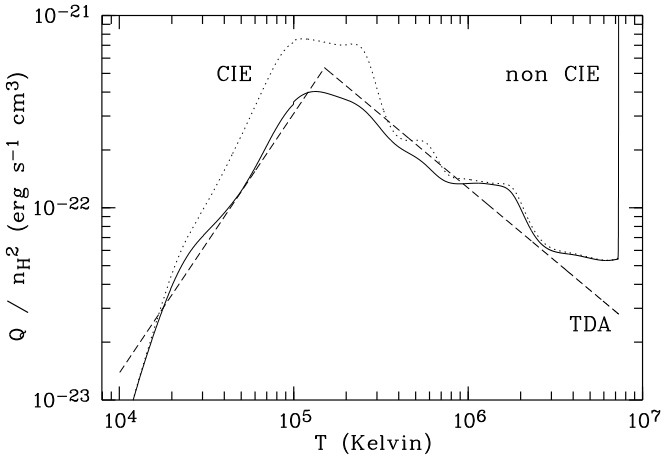

Fig. 8. Plot of the cooling rates (Q/n_H^2 in erg s^{-1} cm^{-3}) as a function of the temperature, for the Collisional Ionization Equilibrium (CIE) case (dotted line) and for the non CIE case (solid line). The dashed line curve is a fit to a non CIE cooling curve (Kafatos 1973) used by TDA in their model.

a higher temperature and a lower density. In order to estimate the impact of such a change on the fate of the particles, we now compare the above model (Fig. 6) which closely reproduces TDA's model E, with one which uses our post-shock conditions but keep TDA's simplified cooling function (allowing us to get rid of the influence of using different cooling functions). Temperature and density evolutions for the same test particle as before are displayed in Fig. 7. We derive cooling lengths more than twice as long than those of TDA. We emphasize this difference in $\mathscr{S}_{\rm cooling}$ since it is one of the main observationnal constraints of any bowshock model. Our comparison illustrates well the essential role played by the pressure driven zone (see Sect. 3.2) in the evolution of the particle as well as the high sensitivity of the model to the choice of post-shock conditions.

3.6. Out of equilibrium versus equilibrium ionization

TDA assumed 'Collisional Ionization Equilibrium' (hereafter CIE) for the ionization balance of oxygen. This can be contrasted with the more physical non CIE assumption as implemented in our model (for each element listed in Sect. 2.1) and in which any particle's evolution depends on its past history and on the rates of change of each ionic specie (see Sect. 2.6.2). Within the zones of high radiative cooling (i.e., in the range 2.10^5 K to 10^4), when non CIE effects are taken into account, we find a mean ionization degree of the ions which is systematically higher (memory effect) than in the case of CIE (see Fig. 9). This can at times strongly reduce the efficiency of radiative cooling, lowering the cooling rate of the gas by more than a factor two as, shown in Fig. 8 (see also Sutherland & Dopita 1993). The cooling lengths $\mathscr{S}_{\rm cooling}$ of the particle for CIE and non CIE are 124.9 and 133.2 pc, respectively, and are consistent with the reduced cooling rate. In the non CIE case, this lag behind of the ionization degree has also the important implication that, for the *same* temperature, the ionization fractions and, therefore, the emissivities differ in the non CIE case from that of CIE. Although TDA used a cooling function which, to a first order, corrects for the main effect on the total cooling rate of using CIE (see dashed line in Fig. 8), at the time of calculating the emissivities of each line, only a proper treatment of non CIE effects as done here can ensure deriving an emission line spectrum fully consistent with the more accurate non CIE assumption.

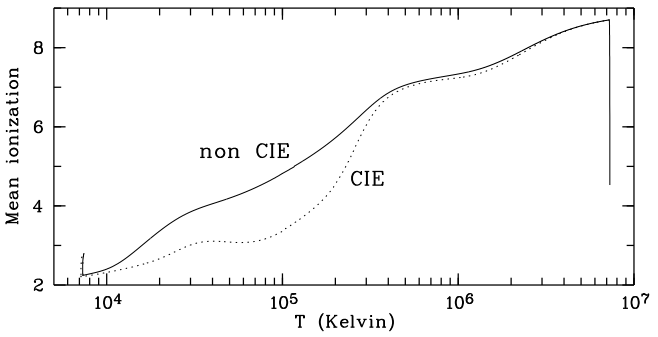

Fig. 9. Mean ionization level of oxygen as a function of temperature, for the Collisional Ionization Equilibrium (CIE) case and for the non CIE case. Note the rapid change in the non CIE mean ionization level just after the shock discontinuity (high temperature end) which results from the rapid ionization of moderately preionized gas (see Sect. 3.2.1.

Table 1. Parameters defining the three models.

ID	C	D_Z	V_o	n_o	$\mathscr{U}_o$	$\mathscr{B}_o$
	-	pc	km.s^{-1}	cm^{-3}	-	μG cm$^{3/2}$
#1	0.6	40	700	1	0.012	3
#2	0.6	40	700	1	0.012	0
#3	0.6	40	700	1	0.001	3

4. Model output - Result example

The model output consists of a file containing the physical (temperature, density, and line emissivities) and geometrical (posi-

Table 2. Example of the evolution of $Z_{cooling}$ as a function of the maximum allowed change rates for our test particle. Note the increase of accuracy along with the number of fluid cells. Changes of less than 0.1 pc fall within the numerical noise of the model.

Maximum allowed change rate				Number	$Z_{cooling}$
T (%)	ϕ (%)	ρ (%)	ρV (%)	of cells	(pc)
1	1	1	1	1452	134.60
0.5	0.5	0.5	0.5	2241	134.06
0.1	0.1	0.1	0.1	10489	133.29
0.05	0.05	0.05	0.05	20911	133.15
0.01	0.01	0.01	0.01	104428	133.17

tion, velocity and volume) characteristics of each (temporal) cell of each (flow) particle (i.e. typically 700-800 particles of 2000-3000 cells each). This allows us to derive not only the global properties of the bowshock (total luminosities, line profiles) but also construct 3D data cubes similar to those obtained with bidimensionnal spectrographs. These results (obtained for various shock velocities, ambient gas densities, ionization and magnetic parameters) will be presented in a second forthcoming paper. In what follows, we will focus on the analysis of the luminosity profiles in the case of three examples (models #1, 2 and 3; see Tab. 1). Note that the model #2 has the same bowshock parameters as in TDA's model E.

4.1. Tuning of the tolerance parameters

The setting of the tolerance parameters of the code (see Sect. 2.6.3) has been made to comply with the following three main constraints: smooth changes of the ionic populations from one fluid cell to the other; falling well within the targetted spectral and spatial resolutions; limiting the computation time. For each model run, the choice of tolerance parameters have been checked against a grid of test particles in which we could trace the accuracy in the evolution of the mean ionization levels of the elements and of the cooling positions $Z_{cooling}$. An example of the change in $Z_{cooling}$ as a function of the maximum allowed rates of change is given in Table 2.

Except for the thermal ionization stage (defined as the first 5.10^3 yr of the particle's evolution) where a high accuracy is required (maximum allowed change rates of 0.01 %), we used the following set of tolerance parameters: maximum allowed change rates of 0.5 % (for T, ρ and ρV) and 0.25 % (for pressure ϕ); velocity sampling of 5 km.s^{-1}; Z sampling of 1 pc. The maximum pressure change rate must be lower than the others because it governs the sampling of the pressure driven stage Sect. 3.2) for which a lowering of the accuracy quickly affects the derived cooling position.

4.2. Cooling length

Fig. 10 shows the evolution of the cooling position $Z_{\rm cooling}$ as a function of the entrance position $Z_{\rm shock}$ of the test particle. The overall shape of this curve for model #1 is very similar to

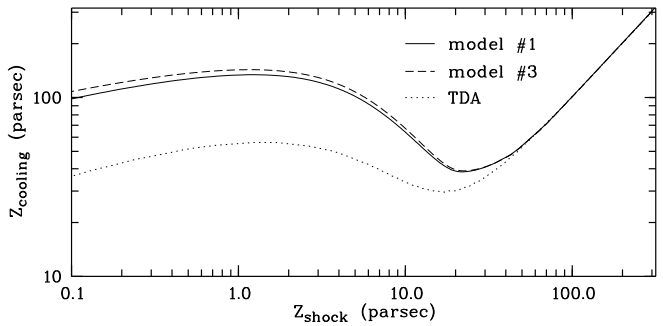

Fig. 10. Cooling distance $Z_{cooling}$ of different test particles as a function of their entrance position Z_{shock} for our models # 1 (solid line), # 3 (dashed line) and for TDA's (dotted line). Cooling distances for the model # 2 are almost identical to those of model # 1 and are not shown.

that of TDA, although displaying much larger cooling lengths for particles with $Z_{\rm shock}$ smaller than a few parsecs. Curves of models #1 and #3 are only slightly different as can be gathered from Fig. 10 while the corresponding curve for model #2 (not shown for clarity) is almost identical to #1. This indicates that neither the nuclear ionizing radiation, nor the magnetic field, significantly affect the evolution of the gas until it has cooled and reached the photionization stage.

Luminosity profiles (for model #1) of lines with very different excitation levels are displayed in Fig. 11 (panels A, C and D). The curves differ markedly in position and shape according to the degree of excitation. Indeed, extremely high excitation lines like [Fe XIV]λ5303 are emitted during the pressure driven stage and show a profile concentrated towards low Z (i.e. higher temperature gas) while somewhat lesser excited lines like [N II]λ6583 or [O III]λ5007 are emitted either during the catastrophic cooling or the photoionization stages. In general, lower excitation lines can be expected to display broader profiles than the high excitation lines (e.g. [O II]$\lambda\lambda$3727, [N II]λ6583).

It is interesting to note the presence of two 'peaks' in the luminosity profiles of [O III]. These are even more striking in the [O III]λ5007 luminosity profile of model #3 (see Fig. 11, panel B) since the contribution of the photoionized gas to the [O III]λ5007 luminosity is much lower than in models #1 or 2. Such peaks take place at the corresponding distances where the $Z_{cooling}$ vs Z_{shock} curve shown in Fig. 10 presents two extrema (e.g. $Z_{shock} \simeq 1$ and 20 pc corresponding to $Z_{cooling} \simeq 40$ and 140 pc, respectively). This was first pointed out by TDA.

Towards larger Z's, the gas is unable to recombine but tends instead towards photoionization equilibrium as a result of the presence of the external ionizing field. Model #1 ($\mathscr{U}$ = 0.012) shows that at larger Z the line emission due to photoionization comes to dominate the profiles of the low and intermediate excitation lines (e.g. [O III]λ5007, [O II]$\lambda\lambda$3727 and [O I]λ6300). A comparison between the [O III]λ5007 luminosity profile of model #1 with #3 (of much smaller $\mathscr{U}$ = 0.001; see Fig. 11, pannel B) illustrates well the role played by the external ionizing field in our model. This suggests that for a spatially *unresolved* bowshock, it is not technically possible in our model to distin-

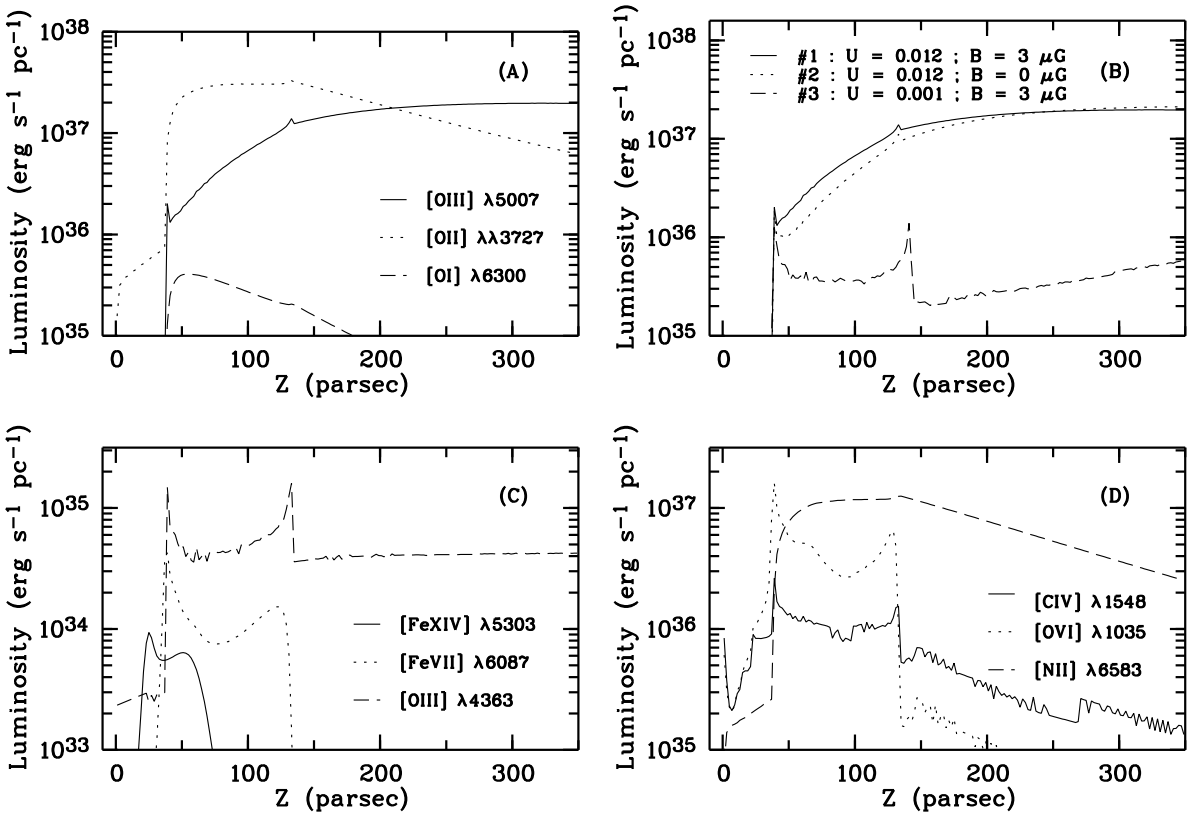

Fig. 11. a [O III]λ5007 (solid line), [O II]λλ3727 (dotted line) and [O I]λ6300 (dashed line) luminosity *profile*s (luminosity per unit of Z after integration across an entire bowshock transversal slice) for model #1. **b** Comparison of the [O III]λ5007 luminosity profile of the three models, #1 (solid line), #2 (dotted line) and #3 (dashed line). **c** [Fe XIV]λ5303 (solid line), [Fe VII]λ6086 (dotted line) and [O III]λ4363 (dashed line) luminosity profiles for model #1. **d** [C IV]λ1549 (solid line), [O VI]λ1035 (dotted line) and [N II]λ6583 (dashed line) luminosity profiles for model # 1.

guish the spectral signature (in terms of line ratios) of the shock from that of photoionization. On the other hand, for spatially *resolved* cases, as in large scale ionized gas in Radio-Galaxies, comparison of the positions of the high and low excitation lines will allow us to put strong constraints on our model as well as on its input parameters.

4.3. Integrated luminosities and line ratios

The integrated luminosities beeing dominated by the emission of the denser and cooler downstream photoionized gas, the bowshock models display rather low excitation spectra as compared to that of the diffuse (preshock) ambient gas. As our model clearly presents two distinct emission zones: shock excited and photoionized, it conforms with the current trend of recent models to invoke more than one component to account for the observed ENLR emission (see review by Morse et al. 1996). For instance, Dopita & Sutherland (1996) have proposed a model in which the photoionized precursor can account for up to half of the Balmer line luminosity while the recent photoionization models of Binette et al. (1996) propose a mixture of matter-bounded and ionization-bounded clouds.

4.4. Bowshock luminosity profiles

A detailed analysis of the behavior of the line ratios as a function of the input parameters of the model will be presented in a forthcoming paper. However, comparison between the three models shown above already reveals interesting trends. First, the overall excitation of the spectra increases with magnetic field (see model #1). Indeed, by lowering the compression factor of the gas, a larger field has the effect of increasing the ionization parameter of the gas during the photionization stage. Also interesting is that as the ionization parameter of the ambient medium is lowered (e.g. model #3), the temperature indicated by the [O III]λ4363/[O III]λ5007 line ratio becomes more representative of collisional excitation (e.g., T_{OIII} = 8300K and 27 000K for models #1 and #3, respectively; c.f. Tab. 3).

4.5. Model limitations

A good review of the limitations of this type model has been already given by TDA in their paper. They are related to the assumptions made either in the hydrodynamical description of the bowshock, or in the computation of the atomic and transfer processes. In the following, we only review the major limitations in regards to our model.

Table 3. Integrated total luminosities (over the range 0-350 pc) relative to Hβ λ4861 for a set of astrophysically interesting lines. Absolute Hβ λ4861 luminosities are: 1.96 10^{39} erg s^{-1}(# 1); 2.83 10^{39} erg s^{-1}(# 2); 1.56 10^{39} erg s^{-1}(# 3).

	Luminosities relative to Hβ λ4861											
Model	[O VI] 1035Å	[C IV] 1548Å	C III] 1909Å	[Ne V] 3425Å	[O II] 3726Å	[Fe V][1] 3856Å	[S II] 4065Å	[O III] 4363Å	He II 4686Å	[O III] 5007Å	[Fe VI][2] 5066Å	[Fe III] 5254Å
# 1	2.6(-1)	1.0(-1)	7.0(-2)	4.8(-3)	3.07	8.1(-3)	1.9(-2)	7.3(-3)	2.3(-1)	2.24	9.0(-4)	2.5(-1)
# 2	1.8(-1)	7.1(-2)	5.2(-2)	3.3(-3)	3.39	4.9(-3)	3.0(-2)	4.9(-3)	1.7(-1)	1.47	6.2(-4)	2.1(-1)
# 3	2.8(-1)	5.5(-2)	7.8(-2)	4.1(-3)	2.40	3.2(-3)	4.1(-2)	4.5(-3)	1.0(-1)	8.0(-2)	8.3(-4)	3.5(-2)

Model	[Fe XIV] 5303Å	[Ca V] 5309Å	[Fe VII] 5721Å	[Fe VII] 6086Å	[Ca V] 6087Å	[O I] 6300Å	[Fe X] 6374Å	Hα 6563Å	[N II] 6583Å	[S II] 6716Å	[S II] 6731Å	[Fe XI] 7889Å
# 1	1.5(-4)	3.3(-5)	4.5(-4)	6.7(-4)	6.5(-6)	2.2(-2)	2.4(-4)	2.93	1.21	3.5(-1)	2.6(-1)	1.7(-4)
# 2	1.1(-4)	2.2(-5)	3.1(-4)	4.7(-4)	4.3(-6)	4.5(-2)	1.7(-4)	2.93	1.37	4.8(-1)	3.9(-1)	1.2(-4)
# 3	1.9(-4)	1.8(-5)	5.2(-4)	7.8(-4)	3.4(-6)	1.3(-1)	3.0(-4)	2.96	1.26	9.7(-1)	7.1(-1)	2.1(-4)

[1] sum of the 3892Å and 3839Å [Fe V] lines.
[2] sum of the 4967Å, 4972Å, 5146Å and 5177Å [Fe VI] lines.

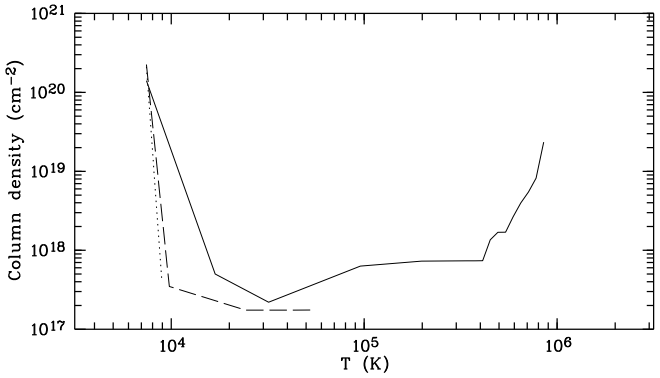

Fig. 12. Temperature stratification of the bowshock layer (model # 1) at three different positions (Z = 100 pc, solid line; Z = 150 pc, dashed line; Z = 200 pc, dotted line). The amount of gas at each temperature is expressed in terms of column density. Note the rapid vanishing of the hot gas component as Z increases.

4.5.1. Hydrodynamical description

First, fixing the geometry of the bowshock and assuming its stationarity completely hides the complexity of the flow which could well rapidly become turbulent (as a result for instance of the growth of Kelvin-Helmoltz instabilities at the tangential discontinuity surface between the shocked ambient medium and the radio material). This is apparent if one compares with hydrodynamical simulations (e.g. Steffen et al. 1996), especially for the tails of the bowshock (high Z) where an expanding cocoon model is much more relevant. Finally, the assumption that the particles do not interact thermally must break down close to the apex where the flow is very slow (stagnation zone).

4.5.2. Internal ionizing sources

By incorporating MAPPINGS IC to the TDA model, we have eliminated most of the drawbacks related to their approximate description of the atomic processes (CIE assumption, absence of charge transfer reactions, approximative cooling rate...). In the present model, however, we still assume that the only ionizing radiation is that produced by the active nucleus, therefore neglecting the contribution of the diffuse ionizing field generated *in situ* within the shock (hard UV line and continuum radiation from the very hot gas). This diffuse radiation could well affect the ionization balance of a fraction of the gas. Dopita & Sutherland (1996) found for instance that a shock velocity of 500 km.s^{-1} internally generates enough radiation to reproduce an ionization parameter of $\simeq 8\ 10^{-3}$, which is comparable to the values inferred from photoionization models of AGN. We emphasize, however, that the infinite slab geometry which they adopted is very different from the thin laminar flow which takes place along our bowshock structure. In practice, the cooler, denser gas layers (i.e. which have already cooled) are effectively exposed only to the nearby outer layers which flow around it. Indeed, we are justified in considering that the photons generated by the hot gas when it is more distant than a few shocked gas layer widths (typically less than ten parsecs) away, either downstream or upstream, can be safely neglected as a result of the large geometrical dilution affecting such UV sources.

On the other hand, even within a few shocked gas layer widths, the amount of diffuse radiation generated appears not to be negligible. As inferred from Fig. 12, the fraction of very hot ($T \simeq 10^6$ K) gas within *nearby* layers and coexisting with the warm emitting line gas, is substantial. To estimate its impact on the ionization balance, we have computed with MAPPINGS IC the hot gas column density, at 10^6 K, which is required to change by ten percent the population of the dominant OIII and OII ions of the warm (10^4 K) gas. The results indicate column densities of order 3 10^{18} and 10^{19} cm^{-2} in the case of OIII with $\mathscr{U}_o$=10^{-2}

and of OII with $\mathscr{U}_o$=10^{-3}, respectively (where $\mathscr{U}_o$ is an estimate of the ionization parameter imposed by the external AGN radiation). These should be compared with the $10^{19}\,\mathrm{cm}^{-2}$ hot gas column density shown in Fig. 12. To conclude, although the amount of diffuse field is certainly not as overbearing as in the infinite slab case, neglecting it altogether is probably an excessive stance and can be considered a caveat of the current models. Having said this, since our warm gas which produces most of the strong optical lines is already photoionized from an infinite supply of external photons, adding additional sources is probably inconsequential to the profile and luminosities of those lines.

5. Conclusion

We have built a bowshock model which provides us with both kinematical and spectral information along the shock structure. This yet unchallenged combination should be a powerful tool to probe the role of shocks in the excitation of the ENLR of active galaxies. Detailed analysis of model grids will be presented in a second forthcoming paper, but we can already emphasize a few salient results: despite their faintness, observations of high excitation level coronal lines like [Fe XIV]λ5303 can put strong constraints on the shock parameters; output spectra are dominated by the photoionized gas line emission and discriminating between shock and photoionization models will require the use of kinematical information in addition to the usual line ratio diagnostics. Comparisons between the predictions of our model and observations of spatially resolved bowshock structures will be the logical straightforward continuation of this work (using either ground based integral field spectrogaphs like TIGER [Bacon et al. 1995] or the Hubble Telescope long-slit capability: STIS).

Appendix A: Mappings Ic

The multipurpose shock/photoionization code MAPPINGS was developed at Mount Stromlo Observatory (see Binette et al. 1985) and has since been maintained and transformed independently over the years by two independent groups. This has lead to very different versions: the branch MAPPINGS I which is maintained by Luc BINETTE (LB) and MAPPINGS II which is maintained by Ralph SUTHERLAND (RS). The two codes share many of the initial routines (e.g. the time-dependent ionization balance algorithm) although, in the most recent versions the transfer of the resonance lines and the dust effects have been developed independently by LB and RS. Moreover, RS has rewritten completely the shock model for his version II (see Sutherland 1993; Sutherland & Dopita 1993; Dopita & Sutherland 1996). One practical advantage of upgrading two codes independently is that the results can at any time be compared to test for possible errors in the implementation of new applications or physical effects or in the updating of atomic physics.

We now proceed to describe the most recent version developped by LB: MAPPINGS IC which is used in deriving the results on bowshock models presented in this paper. The limitation in LB's version I of a maximum of 6 ionization stages has been removed. The version MAPPINGS IC computes the ionization balance over up to 26 ionization stages if or when necessary. However, in any point of a photoionized nebula or of a collisionally ionized gas stream, the ionization stages are calculated in a narrower (but moveable) window of ionization stages: 14 stages in the equilibrium ionization case (e.g. photoionized nebulae) and from 8 to 12 stages in the time-dependent ionization case (e.g. interstellar shocks). The window's position in terms of which ions' abundances are calculated, is determined iteratively and made to cover the most abundant ionic species of each element. MAPPINGS IC now includes iron. All these changes were greatly simplified by the use of the data files compiled by RS for his version II. The collisional ionization coefficients are from Arnaud & Rothenflug (1985). We adopt the collisional excitation rates of hydrogen calculated by Aggarwal et al. (1989).

The treatment of dust effects in MAPPINGS IC (dust scattering, line transfer, photoheating, depletion) remains as defined in version I (Binette et al 1993a, 1993b). Most forbidden line determination are based on a 5-level system except for [O III] and [N II] which use a 6-level structure and [Fe VII] which use a 9-level structure. When the plasma is very hot, the very high ionization lines in the far UV play a major role in determining the cooling function. To compute the effect of those, we included up to 900 lines as tabulated by Landini & Monsignori (1990) (see also Mewe 1985 and references therein). We suspect that the resonance doublet lines in Landini & Monsignori (1990) for [C IV], O VI and N V were not divided by the statistical weight of the ground level. This could explain their cooling being twice as large than ours in the range $10^{4.9} - 10^{5.4}$ K.

References

Acosta-Pulido, J.A., Pérez-Fournon, I., Calvani, M., and Wilson, A.S., 1990, ApJ 365, 119

Acosta-Pulido, J.A., 1993, Ap& SS 205,195

Aggarwal, K.M., Berrington, K. A., Burke, P. G., Kingston, A. E., 1991, J. Phys. B. 24, 1385

Anders, E., Grevesse, N., 1989, Geochim. Cosmochim. Acta 53, 197

Arnaud, M., Rothenflug, R., 1985, A&AS 60, 425

Bacon, R., et al., 1995, A&AS 347, 113

Baldwin et al., 1991, ApJ 374, 580

Binette, L., Dopita, M.A., Tuohy, I.R., 1985, ApJ 297, 476

Binette, L., Fosbury, R. A. E., Parker, D., 1993, PASP 105, 1150

Binette, L., Wang, J. C. L., Zuo, L., Magris, C., M., 1993a, AJ 105, 797

Binette, L., Wang, J., Villar-Martín, M., Martin, P. G., Magris C., M., 1993b, ApJ 414, 535

Binette, L., Wilson, A.S., Storchi-Bergmann T., 1996, A&A 312, 365

Coleman, C.S., Bicknell, G.V., 1985, MNRAS 214, 337

Contini, M., and Aldrovandi, S.M.V., 1983, A&A 127, 15

Contini, M., and Aldrovandi, S.M.V., 1986, A&A 168, 41

Dopita, M. A., Sutherland, R. S., 1996, ApJS 102 161

Dopita, M. A., Sutherland, R. S., 1995, ApJ 455 468

Higgins, S., O'Brien, T., and Dunlop, J., 1995, Ap&SS 233, 311

Kafatos, M., 1973, ApJ 182, 433

Landini, M., Monsignori Fossi, B. C., 1990, A&AS 82, 229

Mewe, R., Gronenschild, E. H. B. M., van den Oord, G. N. J. 1985, A&AS 62, 197
Morse, J.A., Raymond, J.C., Wilson, A.S., 1996, PASP 108, 426
Osterbrock, D. E. 1989, in Astrophysics of Gaseous Nebulae and Active Galactic Nuclei (Mill Valey: University Science Books)
Pedlar, A., Dyson, J.E., 1985, MNRAS 214, 463
Shapiro, P.R., Clocchiatti, A., and Hyesung, K., 1992, ApJ 389, 269
Steffen, W., et al., 1996, MNRAS submitted
Sutherland, R. S., PhD thesis, Australian National University (Canberra), 1993
Sutherland, R. S., Dopita, M. A., 1993, ApJS 88, 253
Sutherland, R. S., Bicknell, G.V., and Dopita, M. A., 1993, ApJ 414, 510
Taylor, D., Dyson, J.E., Axon, D.J., 1992, MNRAS 255, 351
Viegas-Aldrovandi, S.M., and Contini, M., 1989, ApJ 339, 689
Wilson, A.S., and Tsvetanov, Z.I., 1994, AJ 107(4), 1227
Wilson, A.S., Ward, M.J., and Haniff, C.A., 1994, ApJ 334, 121

This article was processed by the author using Springer-Verlag LaTeX A&A style file *L-AA* version 3.